Coupled-channels analyses of scattering and fusion cross sections of $^{16}O + ^{152,154}Sm$, ^{186}W systems at sub- and near-Coulomb barrier energies

T. Izumoto* and T. Udagawa
Department of Physics, University of Texas at Austin, Austin, Texas 78712

B. T. Kim
Department of Physics, Sung Kyun Kwan University, Suwon 440-746, Korea
(Received 22 September 1994)

Coupled-channels calculations are performed to predict fusion, elastic scattering, and inelastic scattering cross sections for the $^{16}O + ^{152,154}Sm$ and $^{16}O + ^{186}W$ systems at sub- and near-Coulomb barrier energies, taking into account the lowest rotational states of the target up to $I^\pi = 8^+$ explicitly. It is shown that experimental data of fusion cross sections taken recently with high precision, partial fusion cross sections, and also average spin values of compound nuclei formed after fusion are well reproduced by the calculations using optical potential parameters that can reproduce elastic and inelastic scattering data. The fusion-barrier distribution, defined as the second derivative of the fusion cross section $d^2(E\sigma)/dE^2$, is also calculated and compared with experimental data. Particular attention is focused on effects of the Y_4 deformation of the target on various physical quantities.

PACS number(s): 25.70.−z, 24.10.Eq

I. INTRODUCTION

Much attention has been focused in recent years on heavy-ion-induced reactions at near- and sub-Coulomb barrier energies [1], the attention being stimulated by a number of interesting observations made in these reactions, such as enhancement in the fusion cross section $\sigma_F(E)$ [2], correlation between the magnitude of $\sigma_F(E)$ and the total direct reaction (DR) cross section σ_{DR} [3], and the threshold anomaly [4], i.e., a rather striking energy dependence of the optical potential for elastic scattering in the above energy region. All these observations hinted at the importance of entrance channel coupling to DR channels. A number of large scale coupled-channels (CC) calculations [5–7] have thus been performed. The simultaneous fits obtained to both fusion and scattering data, however, have not been satisfactory; the fits obtained have not been as good as those obtained in the usual CC analyses of the scattering data alone. Very critical tests of the theoretical calculations have, however, remained as yet unfinished, mainly because sufficient, accurate experimental data for making such tests were not available for both fusion and scattering.

Recently, however, very precise measurements of heavy-ion fusion cross sections $\sigma_F(E)$ at energies near and below the Coulomb barrier have been performed for the $^{16}O + ^{154}Sm$ and the $^{16}O + ^{186}W$ systems by Wei and co-workers [8,9], providing valuable data that can be used for making a detailed test of the theoretical predictions. The original motivation of the measurement was to determine reliable values of the so-called fusion-barrier distribution [10] $D(E)$, defined as $D(E) = d^2(E\sigma_F(E))/dE^2$ [11]. In Ref. [11], $D(E)$ was indeed deduced from the measured $\sigma_F(E)$ for both $^{16}O + ^{154}Sm$ and $^{16}O + ^{186}W$ systems. The deduced $D(E)$ showed a characteristic difference in the energy dependence of the $D(E)$ for the $^{16}O + ^{154}Sm$ and $^{16}O + ^{186}W$ systems. The difference was then explained theoretically in terms of the difference between the Y_4 deformations (β_4) of the targets (^{154}Sm and ^{186}W) involved [9].

The theoretical analysis made in Ref. [9] used an adiabatic approximation [12], and perhaps because of this a rather large diffuseness parameter of a=1.27 fm was called for in reproducing the experimental $\sigma_F(E)$ and $D(E)$. Further, for the case of the $^{16}O + ^{186}W$ system, use was required of β_2 and β_4 values which are significantly different from those determined from analyses of inelastic scattering data. The implication is that the potential and deformation parameters assumed in Ref. [9] may not reproduce the elastic and inelastic scattering data.

The aim of the present study is to perform an extended CC analysis [6,13] of the fusion cross sections of Refs. [8,9], together with elastic and inelastic scattering data [14–16] for the $^{16}O + ^{152,154}Sm$ and $^{16}O + ^{186}W$ systems. Data of partial fusion cross sections [17] and average spin of the fused systems [17,18] will also be considered in the analysis. In the extended CC approach [6,13], the fusion and other direct reactions (mainly particle-transfer reactions that are not taken into account explicitly in the calculations) are described in terms of the imaginary part of the optical potential; the imaginary part thus consists of two parts, i.e., the fusion part and the direct reaction (DR) part. This enables us to treat fusion within the framework of the CC theory. The radius and diffuseness parameters of the fusion potential (the

*Present address: Faculty of General Education, Rikkyo University, Tokyo 171, Japan.

fusion part of the absorptive potential) are fixed from a fit of the calculated fusion cross sections to the data. As will be seen, the radius parameter r_F of the fusion potential thus determined turns out to be $r_F \approx 1.4$ fm. The value is much larger than the value $r_F \approx 1.0$ fm assumed in previous CC calculations performed so far [5–7]. In the calculations, we also take into account the effect of the threshold anomaly [4]. The major issue in the present study is thus whether the CC calculations assuming a large fusion radius parameter can improve the simultaneous fit to the fusion and scattering obtained before in the CC calculations with a small radius parameter.

In what follows, we shall first briefly describe in Sec. II the method of our CC calculations. We employ a new approach for solving the CC equations, which will be discussed in this section. The results of the numerical calculations and the comparison with experimental data are presented in Sec. III. Section IV concludes the paper.

II. THEORY

A. Coupled-channels equations

In the extended CC theory of Refs. [6,13], one performs usual CC calculations for generating the CC wave functions as described, for instance, in Ref. [19]. The wave functions may be written as

$$|\Psi^{(+)}\rangle = \frac{\sqrt{4\pi}}{kr} \sum_{\ell\ell' I'} \hat{\ell}(i^{\ell'} Y_{\ell'} \otimes \Phi_{I'})_{\ell m=0} \chi^{(+)}_{(\ell' I')\ell}(r), \quad (2.1)$$

where $(i^{\ell'} Y_{\ell'} \otimes \Phi_{I'})_{\ell m}$ is the channel wave function of the total angular momentum and its projection (ℓm), $Y_{\ell' m'}$ and $\Phi_{I' M'}$ being the spherical harmonics and the intrinsic wave function of the colliding ions. The $Y_{\ell' m'}$, of course, represents the relative orbital angular motion of the two colliding ions. The radial wave function $\chi^{(+)}_{(\ell' I')\ell}(r)$ in Eq. (2.1) satisfies [19]

$$(E - T - U_0)\chi^{(+)}_{(\ell' I')\ell}(r) = \sum_{\ell''} U_{\ell'\ell''}(r) \chi^{(+)}_{(\ell'' I'')\ell}(r), \quad (2.2)$$

where

$$U_{\ell'\ell''}(r) = \langle (i^{\ell'} Y_{\ell'} \otimes \Phi_{I'})_\ell | U_1 | (i^{\ell''} Y_{\ell''} \otimes \Phi_{I''})_\ell \rangle. \quad (2.3)$$

In the present study, we take into account for $\Phi_{I' M'}$ the lowest rotational states of the target up to $I^\pi = 8^+$ explicitly. The projectile excitation is ignored. We also take into account effects of Coulomb excitations. The diagonal potential U_0 in Eq. (2.2) and the coupling potential U_1 in Eq. (2.3) are generated by following the usual deformed optical potential prescription [19]:

$$U_0 = \frac{1}{\sqrt{4\pi}} U^{(0)(\mathrm{rot})}_{\mathrm{cp}}(r, E), \quad (2.4)$$

$$U_1 = \sum_{\lambda\mu(\lambda\neq 0)} U^{(\lambda)(\mathrm{rot})}_{\mathrm{cp}}(r, E) D^{\lambda}_{\mu 0} Y_{\lambda\mu}(\theta, \phi), \quad (2.5)$$

where

$$U^{(\lambda)(\mathrm{rot})}_{\mathrm{cp}}(r, E) = 4\pi \int_0^1 U(r, E; \theta') Y_{\lambda\mu}(\theta') d(\cos\theta'), \quad (2.6)$$

with

$$U(r, E) = V(r, E) + iW(r, E). \quad (2.7)$$

The θ' dependence involved in the potential $U(r, E)$ in Eq. (2.6) is introduced when the various radii involved in $U(r, E)$ are deformed [see Eq. (2.18) and Eq. (2.19) given below], $V(r, E)$ and $W(r, E)$ being the real and imaginary parts of $U(r, E)$.

The $V(r, E)$ that we use in the present study may be written as follows:

$$V(r, E) = V(r) + \Delta V(r, E) + V_{\mathrm{Coul}}(r), \quad (2.8)$$

where the sum of the first two terms represents the nuclear part of the potential, while the third is the Coulomb part. The nuclear potential consists of the energy-independent part $V(r)$ and the energy-dependent part $\Delta V(r, E)$. We fix $V(r)$ at an energy E_S above the Coulomb barrier, where the scattering cross sections are more sensitive to the parameters than otherwise. $\Delta V(r, E)$ is generated from $W(r, E)$ by using the dispersion relation [20]. Explicitly, the three terms in Eq. (2.8) are given as

$$V(r) = \frac{V_0}{1 + \exp[(r - R_V)/a_V]}, \quad (2.9)$$

$$\Delta V(r, E) = \frac{P}{\pi} \int_0^\infty \frac{W(r, E') dE'}{(E' - E_S)(E' - E)}, \quad (2.10)$$

$$V_{\mathrm{Coul}}(r, R_C) = \frac{3ZZ'e^2}{4\pi R_C^3} \int \frac{\theta(R_C - r')}{|r - r'|} dr'. \quad (2.11)$$

In order to evaluate the fusion cross section, the imaginary part $W(r, E)$ is divided into two portions, a direct reaction part W_{TR} and a fusion part W_F [13]. We have thus

$$W(r, E) = W_F(r, E) + W_{\mathrm{TR}}(r). \quad (2.12)$$

W_{TR} describes absorption due to direct reactions to all other channels than those included explicitly in the calculations, while W_F describes the absorption due to fusion. Note that use is made of the suffix TR, instead of DR for representing the DR part, since the major part comes from the transfer reactions (TR's). The detailed forms of $W_F(r, E)$ and $W_{\mathrm{TR}}(r)$ are

$$W_{\mathrm{TR}}(r, E) = \{1 - \xi(r, E_S)\} W(r), \quad (2.13)$$

$$W_F(r, E) = \xi(r, E) W(r), \quad (2.14)$$

where

$$W(r) = \frac{W_0}{1 + \exp[(r - R_W)/a_W]}, \quad (2.15)$$

$$\xi(r, E) = \frac{\exp[(E - E_B)/a_B]}{\{1 + \exp[(E - E_B)/a_B]\}} \times \frac{1}{1 + \exp[(r - R_F)/a_F]}, \quad (2.16)$$

Note that $W_{\rm TR}(r)$ is assumed to be energy independent and is determined at $E = E_S$. Also note that at $E = E_S$, the sum of $W_F(r,E)$ and $W_{\rm TR}(r)$ becomes simply equal to the energy-independent $W(r)$ defined by Eq. (2.15). Therefore we have at $E = E_S$

$$U(r,E_S) = V(r) + V_{\rm Coul}(r) + iW(r). \tag{2.17}$$

The idea is that we take $U(r,E_S)$ from the literature that gives results determined from the usual CC analysis of the elastic and inelastic scattering data. We then separate $W(r)$ into W_F and $W_{\rm TR}$ parts by means of the radial cutoff factor $1/\{1+\exp[(r-R_F)/a_F]\}$ in $\xi(r,E)$, R_F and a_F being the radius and diffuseness parameters. The additional E-dependent factor involved in the function $\xi(r,E)$, i.e., $1/\{1+\exp[(E-E_B)/a_B]\}$, is designed to introduce an energy dependence in $W_F(r,E)$ in order to take into account the fact that the fusion channels become progressively closed as the incident energy decreases ("threshold anomaly" [4]). Note that E_B in the factor denotes the Coulomb barrier energy and a_B is the the diffuseness.

As remarked, the θ' dependence of $U(r,E)$ is introduced by deforming all the radii involved in $U(r,E)$:

$$R_i = R_{0i}\left(1+\sum_\lambda \beta_\lambda^{(N)} Y_{\lambda 0}(\theta')\right), \tag{2.18}$$

$$R_C = R_{0C}\left(1+\sum_\lambda \beta_\lambda^{(C)} Y_{\lambda 0}(\theta')\right), \tag{2.19}$$

where $i = V$, W, and F, and $\beta_\lambda^{(N)}$ and $\beta_\lambda^{(C)}$ are nuclear and Coulomb deformation parameters, respectively. The values of the nuclear deformation parameters β_λ^N's are obtained from the Coulomb deformation parameters β_λ^C's by taking into account the so-called radius correction for heavy ions [21]:

$$\beta_L^N = \frac{r_C}{r_V}\left\{\beta_L^C + \frac{\delta}{1+\delta}\sum_{i,j} C_{i,j}^L \beta_i^C \beta_j^C\right\}, \tag{2.20}$$

$$r_V = r_C\left\{1+\delta+\frac{\delta}{1+\delta}\sum_{i,j} C_{i,j}^0 \beta_i^C \beta_j^C\right\}, \tag{2.21}$$

where r_C and r_V are, respectively, the Coulomb and real nuclear potential radius parameters and $C_{i,j}^L$ is a geometrical factor:

$$C_{i,j}^L = \begin{cases} \frac{i(i+1)}{8\pi}\delta_{i,j} & \text{if } L=0, \\ -\frac{1}{2}\sqrt{\frac{i(i+1)(2i+1)j(j+1)(2j+1)}{4\pi(2L+1)}} & \\ \times(ij1-1|L0)(ij00|L0) & \text{otherwise.} \end{cases} \tag{2.22}$$

The value of δ is determined from Eq. (2.21).

B. Fusion and transfer cross sections and average spin values

Once $W(r,E)$ is separated into two parts, as in Eq. (2.12), the total reaction cross section σ_R can be given as

$$\sigma_R = \sigma_{\rm IN} + \sigma_{\rm TR} + \sigma_F, \tag{2.23}$$

where $\sigma_{\rm IN}$ is the total inelastic cross section to the channels that are taken into account explicitly in the calculations, while $\sigma_{\rm TR}$ and σ_F are contributions coming from absorption due to, respectively, $W_{\rm TR}$ and W_F. The σ_j (j = TR and F) can be given in terms of W_j and the CC wave function $\Psi^{(+)}$ [6,13] as

$$\begin{aligned}\sigma_j &= \frac{2}{\hbar v}\langle\Psi^{(+)}|W_j|\Psi^{(+)}\rangle \\ &= \frac{2}{\hbar v}\sum_{\alpha,\beta}\langle\chi_\beta^{(+)}|(W_j)_{\beta\alpha}|\chi_\alpha^{(+)}\rangle \\ &= \sum_\ell \sigma_j(\ell),\end{aligned} \tag{2.24}$$

where

$$\sigma_j(\ell) = \frac{\pi(2\ell+1)}{k^2}\left(\frac{8}{\hbar v}\right) \times \sum_{I'I''\ell'\ell''}\int_0^\infty \chi_{(\ell''I'')\ell}^{(+)*} W_{j;\ell''\ell'}(r)\chi_{(\ell'I')\ell}^{(+)}(r)dr, \tag{2.25}$$

$$W_{j;\ell''\ell'}(r) = \langle i^{\ell''}(Y_{\ell''}\times\Phi_{I''})_\ell|W_j|i^{\ell'}(Y_{\ell'}\times\Phi_{I'})_\ell\rangle. \tag{2.26}$$

Note that W_j includes not only diagonal, but also nondiagonal coupling terms.

The average kth moment of the spin distribution of the compound nucleus is calculated by using the partial cross sections $\sigma_F(L=\ell)$ as

$$\langle L^k\rangle = \sum_L L^k\sigma_F(L)/\sum_L \sigma_F(L). \tag{2.27}$$

C. Method of solution of the CC equations

The dimension of the CC equations we solve in the present study is fairly large; in fact, taking into account the rotational states of the target up to $I^\pi = 8^+$, it becomes $N = 25$. This, together with the inclusion of Coulomb excitation, makes the numerical calculations very time consuming. In order to reduce the computation time, we solve here the CC equations by following a method developed previously for solving continuum random-phase-approximation equations [22] and also nonlocal optical potential problems [23]. We give below a brief description of the method.

The first step is to convert the differential equation [as given by Eq. (2.2)] into an integral form. For an example, Eq. (2.2) may be rewritten (in an abbreviated form) as

$$|\chi_\ell\rangle = |\chi_\ell^{(0)}\rangle\delta_{\ell\ell_0} + \sum_{\ell'} G_\ell^{(0)} U_{\ell\ell'}|\chi_{\ell'}\rangle, \tag{2.28}$$

where $G_\ell^{(0)}$ is the optical model Green's function and is given by

$$G_\ell^{(0)} = \frac{1}{E-T-U_0+i\epsilon}. \tag{2.29}$$

We further transform Eq. (2.28) by multiplying both sides by $U_{\ell'\ell''}$ and summing over ℓ'' into

$$|\Lambda_{\ell'}\rangle = |\rho_{\ell'}\rangle + \sum_{\ell''} U_{\ell'\ell''} G^{(0)}_{\ell''} |\Lambda_{\ell''}\rangle, \tag{2.30}$$

where

$$|\Lambda_{\ell'}\rangle = \sum_{\ell''} U_{\ell'\ell''} |\chi_{\ell''}\rangle, \tag{2.31}$$

$$|\rho_{\ell'}\rangle = \sum_{\ell''} U_{\ell'\ell''} |\chi^{(0)}_{\ell''}\rangle \delta_{\ell'',\ell_0} = U_{\ell'\ell_0} |\chi^{(0)}_{\ell_0}\rangle. \tag{2.32}$$

Equation (2.30) is our basic equation to be solved. Once $|\Lambda_\ell\rangle$ is solved, we may easily evaluate $|\chi_\ell\rangle$ as

$$|\chi_\ell\rangle = |\chi^{(0)}_\ell\rangle \delta_{\ell\ell_0} + \sum_{\ell'} G^{(0)}_\ell |\Lambda_\ell\rangle. \tag{2.33}$$

The above equation follows from the insertion of Eq. (2.31) into Eq. (2.28).

The merit of considering Eq. (2.30), instead of Eq. (2.28), is in the fact that the unknown quantities $|\Lambda_{\ell'}\rangle$ are localized functions, in contrast to $|\chi_\ell\rangle$, which are of course not localized. We may then assume that $|\Lambda_{\ell'}\rangle$ can be expressed as a sum of a set of orthonormalized basic functions $\{|D_i\rangle\}$ (Lanczos method),

$$|\Lambda\rangle = \sum_{i=0}^{N} C_i |D_i\rangle. \tag{2.34}$$

The basic functions are generated as follows:

$$|D_0\rangle = \frac{1}{N_0}|\rho\rangle, \tag{2.35}$$

$$|D_{i+1}\rangle = \frac{1}{N_{i+1}} \left\{ UG^{(0)}|D_i\rangle - \sum_{j=0}^{i} \alpha_{ij}|D_j\rangle \right\}, \tag{2.36}$$

where α_{ij} is fixed from the orthonormal condition

$$\langle \tilde{D}_j | D_i \rangle = \delta_{ij}. \tag{2.37}$$

Equation (2.30) is then reduced to the following inhomogeneous linear equation for determining the expansion coefficients $C_i (i = 1 \sim N)$:

$$\sum_{i=0}^{N} (\delta_{ji} - \alpha_{ij}) C_i = N_0 \delta_{j0}. \tag{2.38}$$

The convergence of the expansion, i.e., whether we have taken into account enough basic functions in the expansion or not, may be checked, e.g., with $\epsilon = 10^{-3}$ as

$$C_N \leq \epsilon |C_{N-1}|. \tag{2.39}$$

The essential task of the numerical calculations involved in the above approach lies in evaluation of the integral for generating the basic functions, i.e., in the calculations of $UG^0|D_i\rangle$. Since we include Coulomb excitation effects, the radial integral involved in the calculation has to be extended to a large distance. We, in fact, carry out the integration up to $r_{\max} = 250$ fm. This makes the calculation very time consuming. In order to save computation time, we employ the semiclassical approximation [24,25], particularly in evaluating the integrals at large distance, say, $r > \sqrt{2}a$, where a is the classical turning point. There the Coulomb wave functions $H^{(\pm)}_\ell(kr)$ are approximated by WKB wave functions and the rapidly oscillating terms in the integrand such as $H^{(+)}_\ell(kr)H^{(+)}_{\ell'}(k'r)$ and $H^{(-)}_\ell(kr)H^{(-)}_{\ell'}(k'r)$ are discarded. Once this approximation is made, one can use a large mesh size in carrying out the integrals, enabling us to save considerably on computation time without losing numerical accuracy in the calculations. We take into account partial waves up to $\ell = 700$. As remarked above, the solutions of the CC equations are obtained by setting up a convergence check with $\epsilon = 10^{-3}$. $N = 55$ is set as the maximum number of iterations. The typical number N necessary for achieving convergence is $N \approx 20$ for the ^{16}O + ^{152,154}Sm systems, while a somewhat larger number N is required for the ^{16}O + ^{186}W system. Sometimes, $N \approx 50$ is required for the latter reaction case.

III. ANALYSIS

A. Optical potential parameters

The parameters of the starting optical potential $U(r, E_S)$ of Eq. (2.17) are taken from Stokstad and Gross [14] for the ^{16}O + ^{152,154}Sm systems at $E_{\rm lab}$ = 72 MeV and from Love *et al.* [26] for the ^{18}O + ^{184}W system at $E_{\rm lab}$ = 90 MeV. Modifications are, however, introduced to the strength parameters V_0 and W_0 in such a way that the resultant elastic and inelastic scattering cross sections fit the data [14,15] as well as possible. Since scattering data are not available for the ^{16}O+^{186}W system, use was made of the data for the ^{18}O + ^{184}W system. This procedure fixs the potential parameters at $E_{\rm lab}$=72 and 90 MeV for the ^{16}O + ^{152,154}Sm and ^{16}O+^{186}W systems, respectively. The corresponding

TABLE I. Optical potential parameters.

System	Set	V_0 (MeV)	W_0 (MeV)	r_V (fm)	r_W (fm)	a_V (fm)	a_W (fm)	r_C (fm)
^{16}O + ^{152,154}Sm	A	20.0	20.0	1.34	1.34	0.57	0.36	1.25
^{16}O + ^{152,154}Sm	B	22.5	13.0	1.34	1.34	0.57	0.36	1.25
^{16,18}O + ^{186,184}W	A	40.0	13.5	1.313	1.313	0.457	0.457	1.10
^{16,18}O + ^{186,184}W	B	35.0	18.0	1.313	1.313	0.457	0.457	1.10

TABLE II. Fusion potential parameters.

System	Set	r_F (fm)	a_F (fm)	E_B (MeV)	a_B (MeV)
$^{16}O + {}^{152,154}Sm$	A	1.51	0.30	59.0	3.0
$^{16}O + {}^{152,154}Sm$	B	1.47	0.30	59.0	3.0
$^{16}O + {}^{186}W$	A	1.45	0.30	69.0	3.25
$^{16}O + {}^{186}W$	B	1.48	0.30	69.0	3.25

c.m. energies (65 and 83 MeV, respectively) are called E_S values for these two systems. The set A values of the parameters listed in Table I are those determined in this way. We shall also perform, however, calculations of σ_F with another set B in order to study the sensitivity of σ_F to the choice of the potential. Set B can also reproduce quite well the scattering data, though the fit obtained is somewhat worse than that obtained with set A. Set B is also listed in Table I.

The parameters r_F and a_F in $W_F(r, E)$ are determined by demanding that $\sigma_F(E)$ at the incident energy E_S (which is above the Coulomb barrier) should be reproduced. The values thus determined for the set A and B potentials are listed in Table II. We note that the values of $r_F \approx 1.4$ fm and $a_F = 0.3$ fm thus fixed are very much the same as those determined previously in an extended optical model analysis [27] of the elastic scattering and fusion data. It is remarkable that the value of r_F is much larger than that used in CC calculations done before [5–7].

As for the parameters E_B and a_B describing the energy dependence of the fusion potential $W_F(r, E)$, we set E_B equal to the height of the Coulomb barrier. The diffuseness parameter a_B is fixed as given in Table II. (The parameter a_B is not critical in the present calculations.) We normalized the dispersive term $\Delta V(r, E)$ of the real part [20] to be zero at $E_{\text{c.m.}} = E_S$. In Fig. 1, we show energy dependence of the real and imaginary parts of the nuclear optical potential at three radial distances at the surface region.

B. Elastic and inelastic scattering

Figure 2 shows a comparison of the calculated elastic and inelastic scattering cross sections to the data at $E = E_S$. Use is made in the calculations of the set A optical potential parameters (see Table I) and also of the Coulomb deformation parameters listed in Table III. The values of β_λ^C's for the $^{16}O + {}^{152,154}Sm$ systems are taken from Refs. [14,21], while those for the $^{18}O + {}^{184}W$ and $^{16}O + {}^{186}W$ systems are from Refs. [26,28]. The nuclear deformation parameters are then generated by using Eq. (2.20). These values are further modified by applying the radius correction for heavy ions [21]. Note that the signs of β_4 for the Sm isotopes are positive, while those for the W isotopes are negative. These signs are well established from α-particle scattering experiments [21]. The solid lines shown in Fig. 2 are the final theoretical predictions, while the dashed lines shown there are 4^+ cross sections obtained by artificially reversing the sign of β_4.

The overall fit of the calculated cross sections to the data is very good as expected. We note that in order to get this good fit, it was important to use a positive β_4 for ^{152}Sm and a negative β_4 for ^{184}W. This is clearly seen in the case of the $^{16}O + {}^{152}Sm$ system; the calculated 4^+ cross section changes quite dramatically when the sign of β_4 is reversed as demonstrated by the dotted line in the figure. The change occurs as a consequence of the change in the interference between the double $\Delta L = 2$ and single $\Delta L = 4$ excitations. The good fit of the calculated 4^+ angular distribution with positive β_4 to the experimental

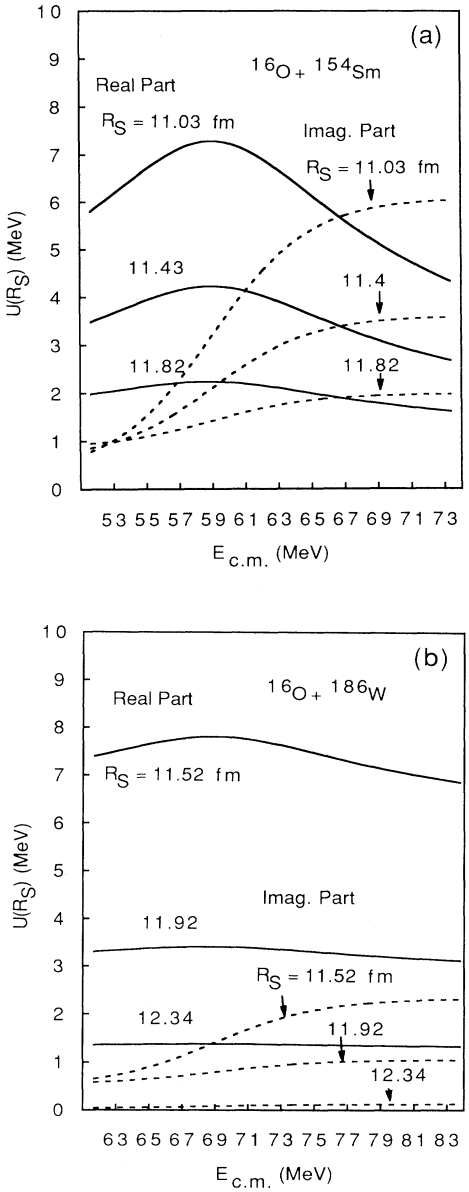

FIG. 1. Energy dependence of the real and imaginary parts $V(R_s, E)$ and $W(R_s, E)$ of the nuclear optical potential (a) for the $^{16}O + {}^{154}Sm$ system ($A = 154$) and (b) for the $^{16}O + {}^{186}W$ system ($A = 186$), calculated at three radial distances $R_s = 1.40$, 1.45, and 1.50 times of $(16^{1/3} + A^{1/3})$ fm. Here the nuclear deformation β_λ^N's are set to be zero.

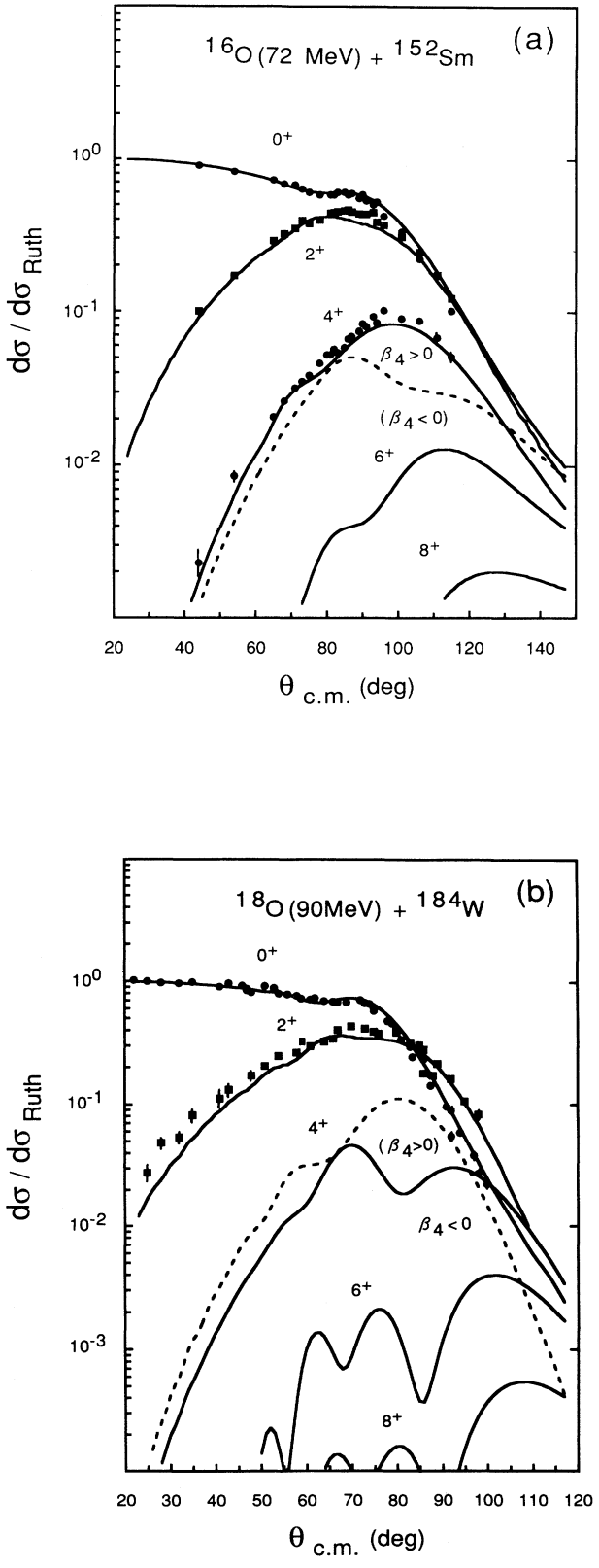

FIG. 2. Calculated elastic and inelastic scattering cross sections (a) for ^{16}O + ^{152}Sm at $E_{\rm lab}$ = 72 MeV and (b) for ^{18}O + ^{184}W at $E_{\rm lab}$ = 90 MeV in comparison with the experimental data of Refs. [14] and [15], respectively.

TABLE III. Coulomb deformation parameters.

	β_2^C	β_4^C	β_6^C
^{152}Sm	0.25	0.048	-0.009
^{154}Sm	0.27	0.054	-0.014
^{184}W	0.280	-0.089	0.0
^{186}W	0.239	-0.090	0.0

data [14] clearly indicates that the sign of β_4 for that system is positive. A similar change is also seen in the 4^+ cross section of the ^{18}O + ^{184}W system. Unfortunately, there is no experimental data available at this moment for this system to test the theoretical prediction. Finally we note that the change of the sign of β_4 affects not only the 4^+ cross section but also the cross sections of other spin states significantly.

Figure 3 shows the results of the calculations for the ^{16}O + ^{152}Sm at other energies $E_{\rm lab}$ = 59, 62, 66, and 68 MeV than $E_{\rm lab}$ = 72 MeV considered above and are compared with the experimental data [16]. The same optical potential parameter set A is used in the calculations. The overall fit of the calculated results to the data is again very good. The fit obtained above is better than that reported previously in Ref. [16]. This supports the validity of the optical potential parameter set A.

For the sake of comparison, we included in Fig. 3 by dashed lines, as was done in Fig. 2, 4^+ cross sections obtained by artificially reversing the sign of β_4. For lower energies, not much difference is observed in the shapes of the cross sections obtained with positive and negative β_4, but still appreciable difference is observed in the magnitude of the cross sections.

C. Fusion cross section

In Figs. 4 and 5, calculated fusion cross sections $\sigma_F(E)$ for the ^{16}O + ^{152,154}Sm and ^{16}O + ^{186}W systems, respectively, are compared with the experimental data [8,9]. It is seen that the calculation reproduces the experimental σ_F very well. We are thus able to achieve a simultaneous fit to both fusion and scattering data. In Figs. 4 and 5, included are calculated $\sigma_R(E)$, $\sigma_{\rm IN}(E)$, and $\sigma_{\rm TR}(E)$. It is remarkable that the calculated $\sigma_{\rm TR}(E)$ decreases much slower than does $\sigma_F(E)$. Such a feature in $\sigma_{\rm TR}(E)$ is indeed observed in the measured $\sigma_{\rm TR}(E)$. Some authors [14] assume that $W(r,E) = W_F(r,E)$ without separating $W(r,E)$ into the F and TR parts. This means that $\sigma_F + \sigma_{\rm TR}$ is identified as σ_F. As seen, this approximation overestimates σ_F by a large factor, particularly at lower energies.

In Fig. 6, we study how the calculated fusion cross sections change if one ignores higher-spin states one by one. It is seen that almost no change is seen when one ignores the highest-spin 8^+ state. We note, however, that the change is not completely negligible, particularly in the barrier distribution $D(E)$ as will be discussed later in Sec. III D.

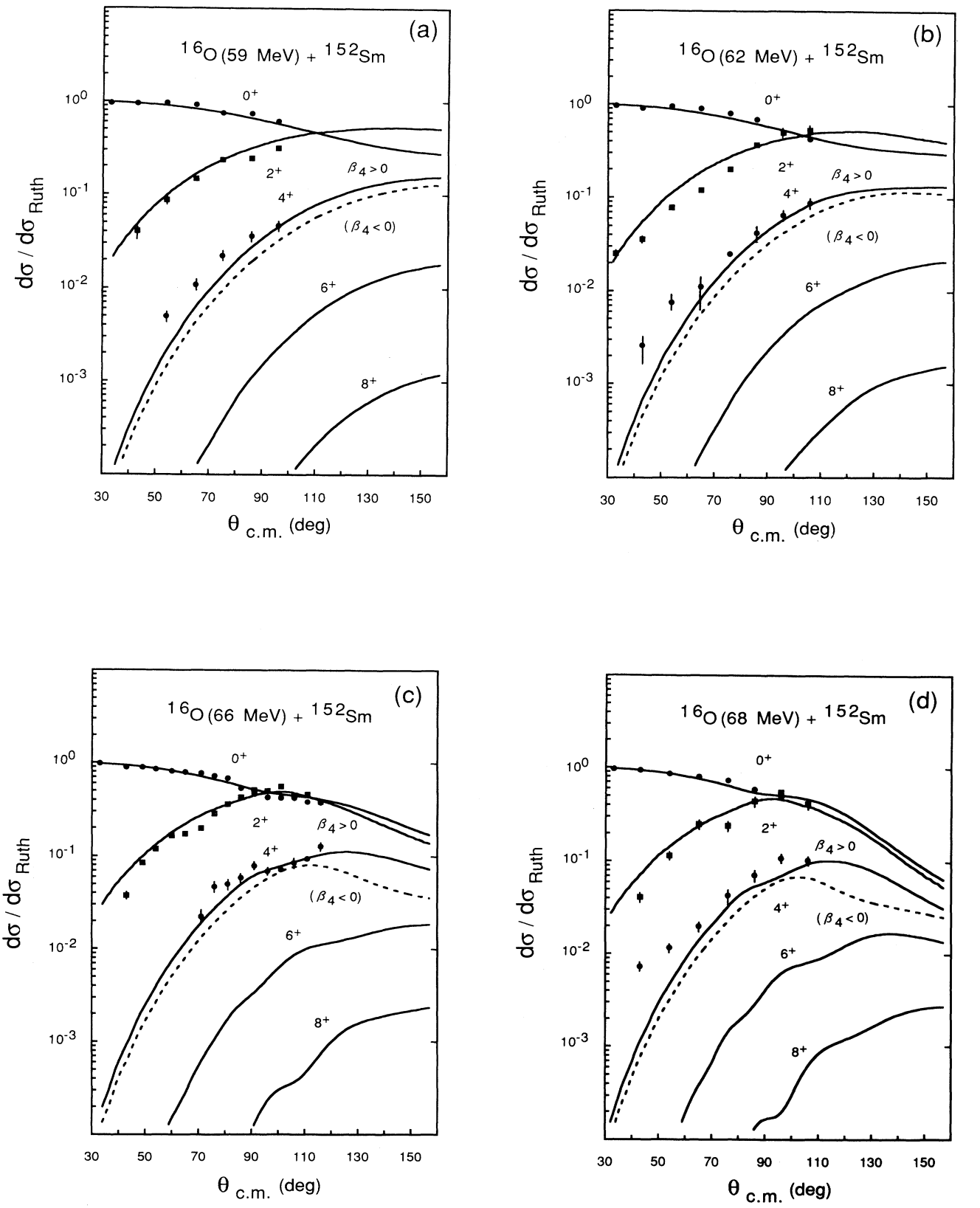

FIG. 3. Comparison of the elastic and inelastic cross sections of ^{16}O from ^{152}Sm from the coupled-channels calculation with the experimental data at $E_{\rm lab}$ = 59, 62, 66, and 68 MeV [16]. The dashed line shows the prediction for the 4^+ state by artificially reversing the sign of β_4.

D. Fusion-barrier distribution

We now turn our attention to the fusion-barrier distribution $D(E)$, which is, in practice, approximated by a finite difference $\delta^2(E\sigma)/\delta E^2$. We use the five-point finite difference formula. In Refs. [8,9], the data of σ_F have been taken with a step size of $\delta E = h$ =0.453 MeV for the ^{16}O + ^{154}Sm system and h =0.460 MeV for the ^{16}O + ^{186}W system. The barrier distribution is, however, normally calculated by using δE=4h. Note that δE=4h $\approx$ 1.8 MeV, which is quite large. The use of such a large δE=4h is required in order to make the statistical error of the deduced $D(E)$ reasonably small [9]. With such a large δE, we are looking at quite gross features of $D(E)$. In the present study, however, we shall investigate $D(E)$ extracted by using δE=h and δE=2h, in addition to the case of δE=4h. When necessary, we shall distinguish these $D(E)$ obtained by using δE=h, 2h, and 4h as $D_h(E)$, $D_{2h}(E)$, and $D_{4h}(E)$, respectively. In Figs. 7 and 8, we first show calculated $D_{4h}(E)$ and $D_{2h}(E)$ by the solid lines in comparison with the corresponding experimental data. The vertical bars indicated in these figures are estimated from the statistical errors of the experimental data. It is seen that the calculated results explain fairly well the experimental data.

It is remarkable that the experimental $D(E)$ of the ^{16}O + ^{154}Sm and ^{16}O + ^{186}W systems are significantly different from each other, particularly at the lower energies; $D(E)$ of the ^{16}O + ^{154}Sm system rises rather slowly at the lower energies while $D(E)$ of the ^{16}O + ^{186}W systems does rather rapidly. This characteristic difference is fairly well explained by the calculations. The sign of β_4 played a crucial role in reproducing the difference; if one changes the sign of β_4, the predicted $D(E)$ becomes completely different as shown in the figures by the dotted lines. It should be noted here that a similar explanation has been given earlier in a study based on the adiabatic approximation [9].

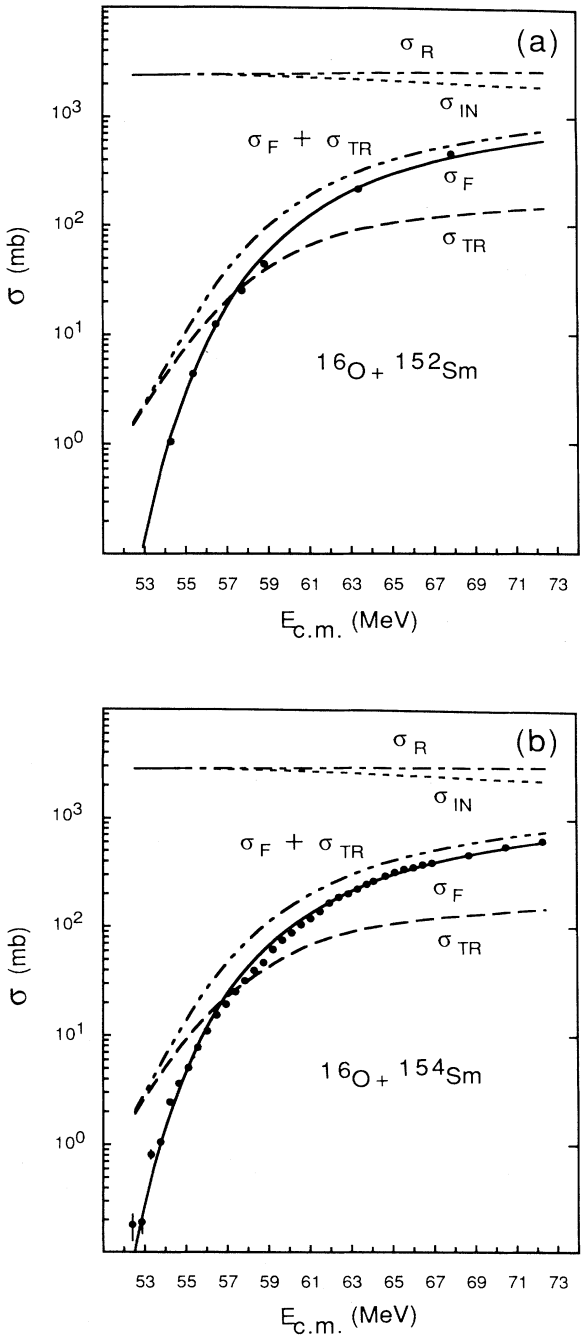

FIG. 4. Calculated fusion cross sections σ_F for the ^{16}O + ^{152,154}Sm systems in comparison with the experimental data. Included also are the reaction cross sections σ_R, the inelastic scattering cross sections $\sigma_{\rm IN}$, and the transfer reaction cross sections $\sigma_{\rm TR}$.

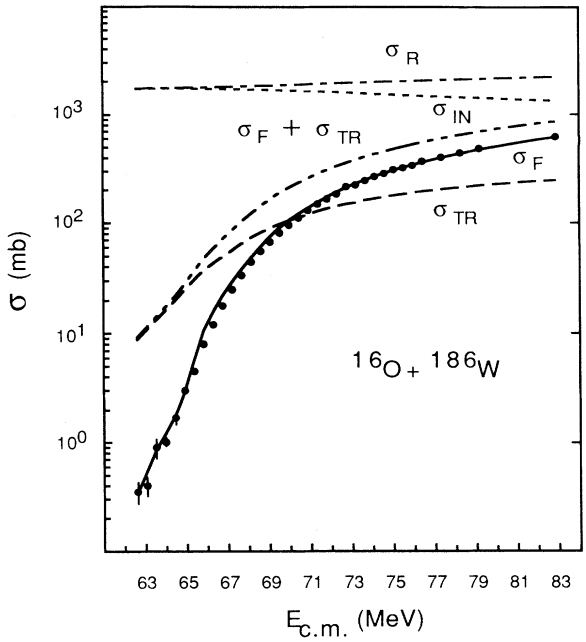

FIG. 5. Calculated fusion cross sections σ_F for the ^{16}O + ^{186}W system in comparison with the experimental data. Included also are the reaction cross sections σ_R, the inelastic scattering cross sections $\sigma_{\rm IN}$, and the transfer reaction cross sections $\sigma_{\rm TR}$.

It is also remarkable that the peak structure appears more conspicuously in $D(E)$ for the $^{16}O + ^{186}W$ system than for the $^{16}O + ^{154}Sm$ system. We may ascribe this to the fact that the absorptive potential for the the $^{16}O + ^{186}W$ system is much weaker by about a factor of 3 at the surface than that for the $^{16}O + ^{154}Sm$ system (see Fig. 1). The stronger absorption averages out the structure. Also, a large negative β_4 for the $^{16}O + ^{186}W$ system plays a crucial role there. This point will further be discussed later when the calculated partial fusion cross section $\sigma_F(\ell)$ is presented.

Also notable is that the structure becomes more remarkable when δE is decreased from $4h$ to $2h$. The reason seems to be evident; the structure should appear more markedly in the $D(E)$ with a smaller δE, since the energy average involved becomes less for the smaller δE.

In Fig. 9, we study how $D(E)$ changes when the coupling schemes of the calculations are changed. For the case of the $^{16}O + ^{154}Sm$ system, two peaks appear when the 0^+-2^+ coupling is assumed, while in the 0^+-2^+-4^+ coupling, the number of the peaks increases to 3. However, even if the 6^+ and 8^+ states are added successively,

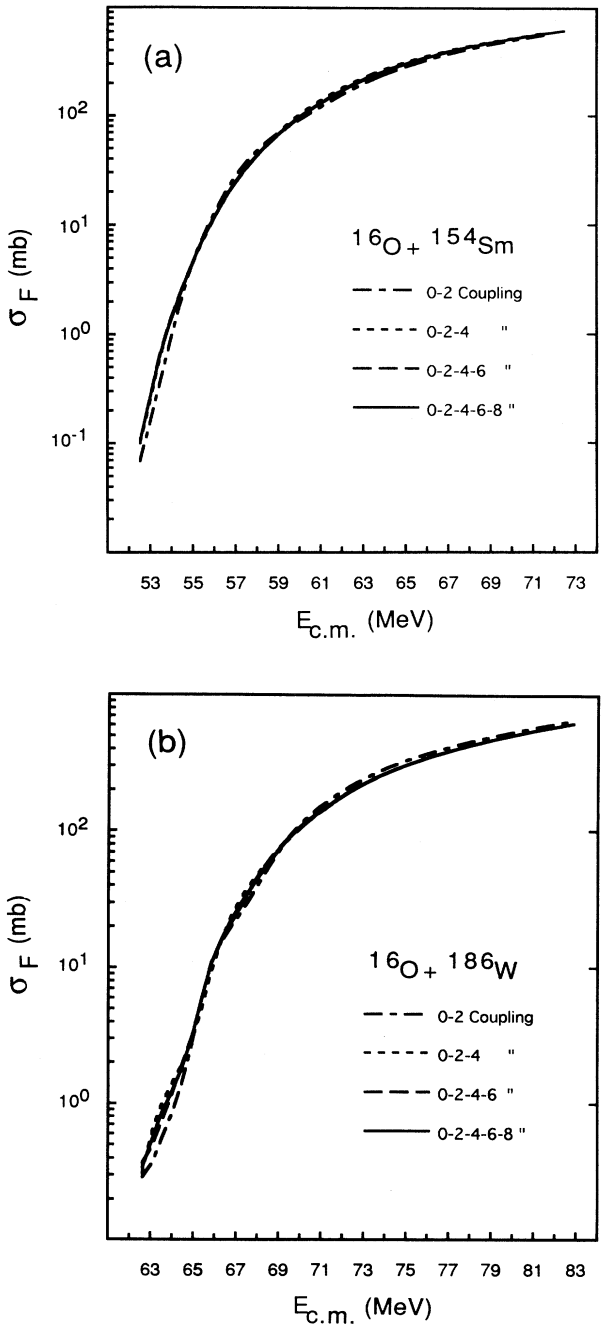

FIG. 6. Fusion cross sections calculated with varied number of excited target states (a) for $^{16}O + ^{152}Sm$ system and (b) for $^{16}O + ^{186}W$ system.

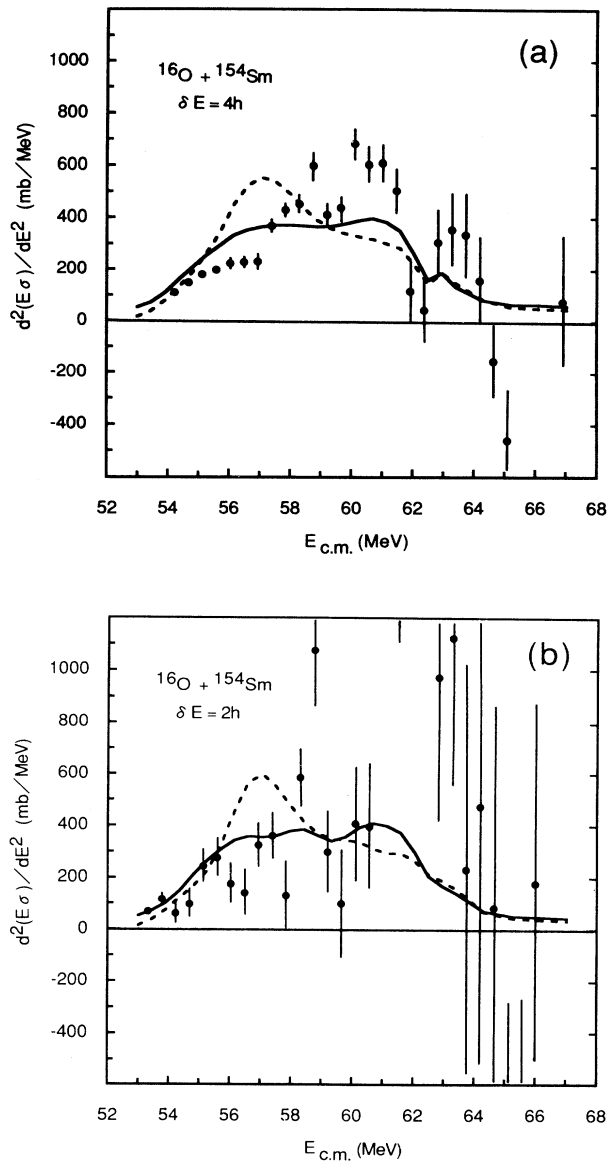

FIG. 7. Calculated $\delta^2(E\sigma)/\delta E^2$ (solid lines) for the $^{16}O + ^{154}Sm$ system in comparison with the data for (a) $\delta E = 4h$ and (b) $\delta E = 2h$. The dashed lines shown are the predictions obtained by reversing the sign of the β_4.

the number of peaks does not increase any more, but rather the peak structure tends to be smoothed out. For the case of the $^{16}O + ^{186}W$ system, the number of peaks appearing is 3 in the 0^+-2^+ coupling case and 4 in 0^+-2^+-4^+ coupling case. We thus have an additional peak for the $^{16}O + ^{186}W$ system. This is in accordance with the tendency seen before that the structure appears more conspicuously in this system. The weak absorption and a large negative β_4 are responsible for the appearance of the additional peak.

In view of the importance of the absorption effects, we show in Fig. 10 calculated $D_{2h}(E)$ with the optical potential parameter set B. The set B potential has a weaker (stronger) absorption for the $^{16}O + ^{152}Sm$ ($^{16}O + ^{186}W$) system than the set A potential has. Comparing with the $D_{2h}(E)$ shown before in Figs. 7 and 8, it is seen that the structure of $D(E)$ shown in Fig. 10 is more distinct for

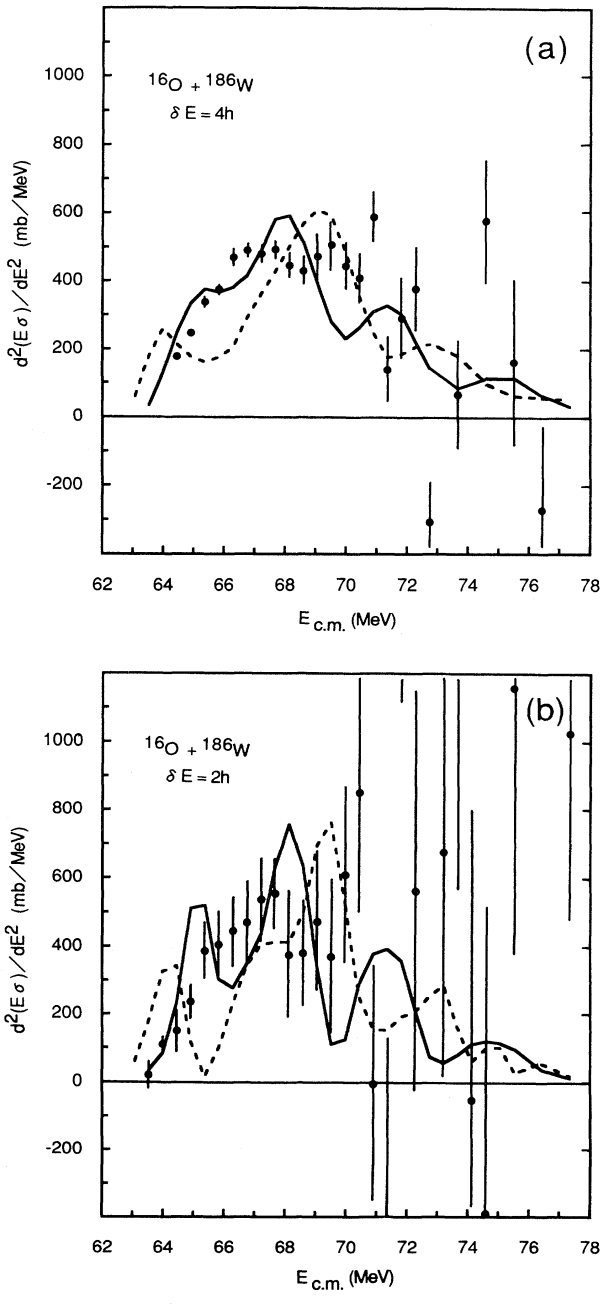

FIG. 8. Calculated $\delta^2(E\sigma)/\delta E^2$ (solid lines) for the $^{16}O + ^{186}W$ system in comparison with the data for (a) $\delta E = 4h$ and (b) $\delta E = 2h$. The dashed lines shown are the predictions obtained by reversing the sign of the β_4.

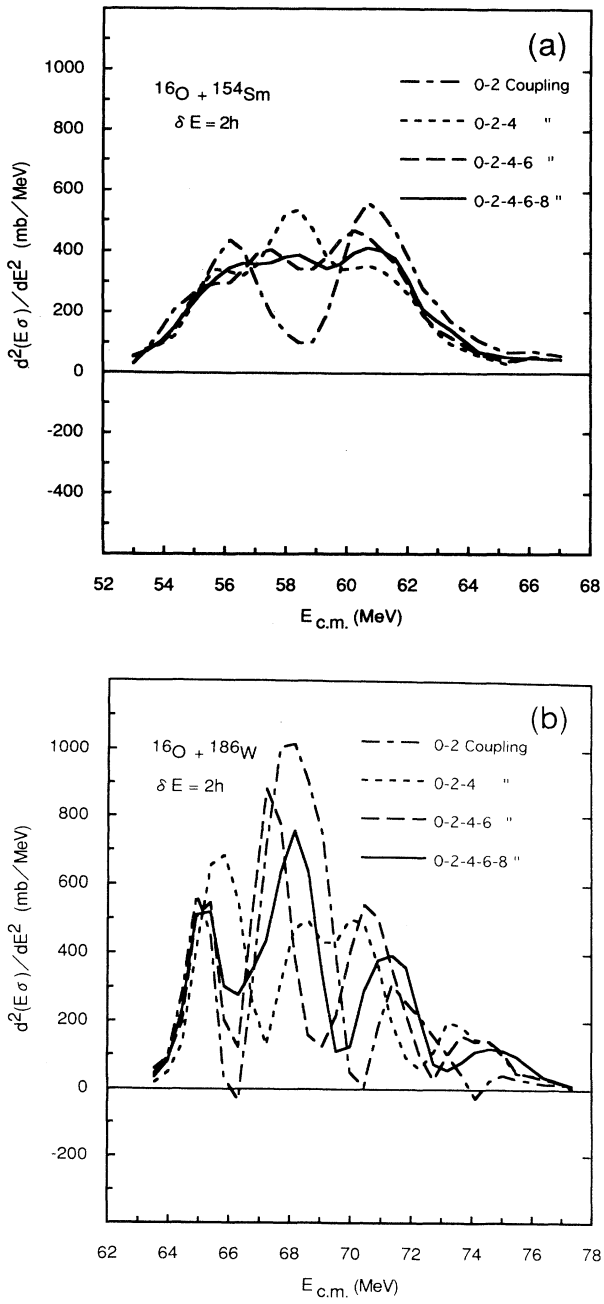

FIG. 9. $\delta^2(E\sigma)/\delta E^2$ calculated with $\delta E = 2h$ for varied number of excited target states (a) for $^{16}O + ^{154}Sm$ system and (b) for $^{16}O + ^{186}W$ system.

the case of the $^{16}O + ^{152}Sm$ system, while the situation is opposite in the $^{16}O + ^{186}W$ system. This shows that the absorption indeed tends to smooth out the structure as it should.

Finally, we show in Fig. 11 calculated $D_h(E)$ in comparison with the experimental data, taking, as an example, the $^{16}O + ^{186}W$ system. As seen, the statistical error bars are quite large, particularly at the higher-energy region. It is thus impossible to make any meaningful physical discussions there. However, at the extremely low-energy side, the statistical errors are relatively small.

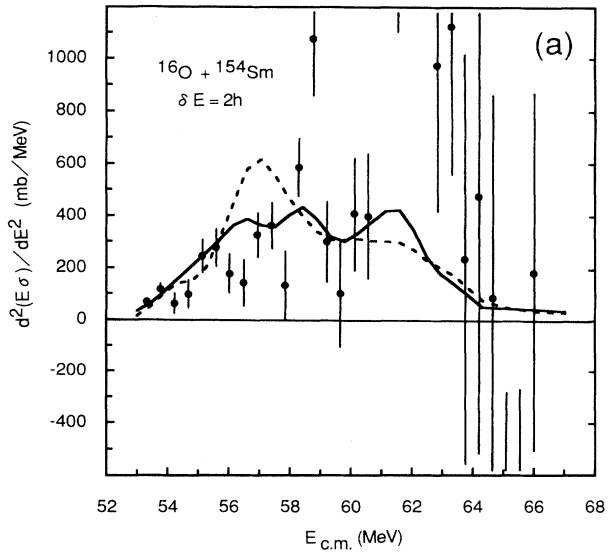

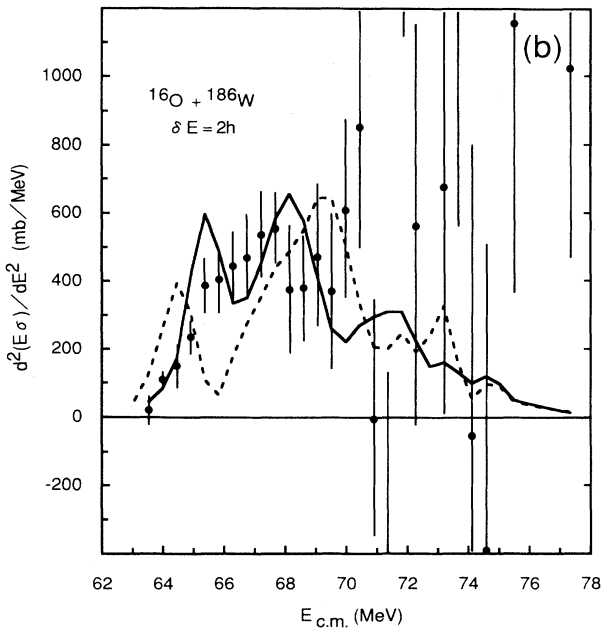

FIG. 10. Calculated $\delta^2(E\sigma)/\delta E^2$ (solid lines) by assuming set B of the optical potential parameters and the $\delta E = 2h$ for (a) $^{16}O + ^{154}Sm$ and (b) $^{16}O + ^{186}W$ systems. The dashed lines are the predictions obtained by reversing the sign of the β_4.

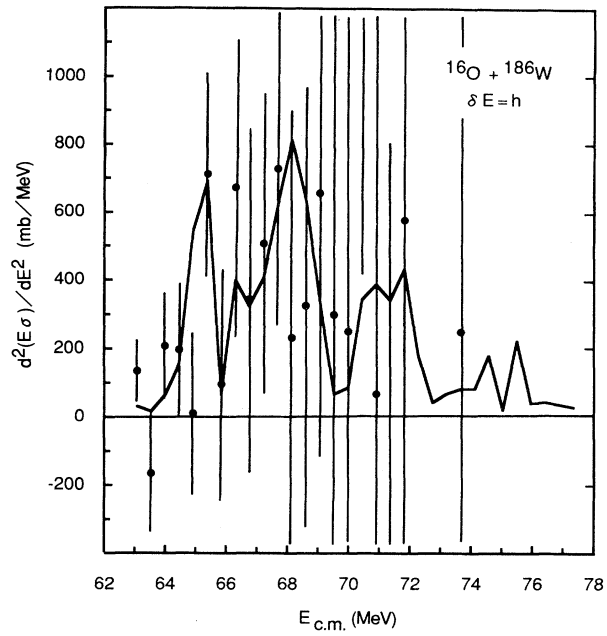

FIG. 11. The calculated $\delta^2(E\sigma)/\delta E^2$ for the $^{16}O + ^{186}W$ system in comparison with the data for $\delta E = h$.

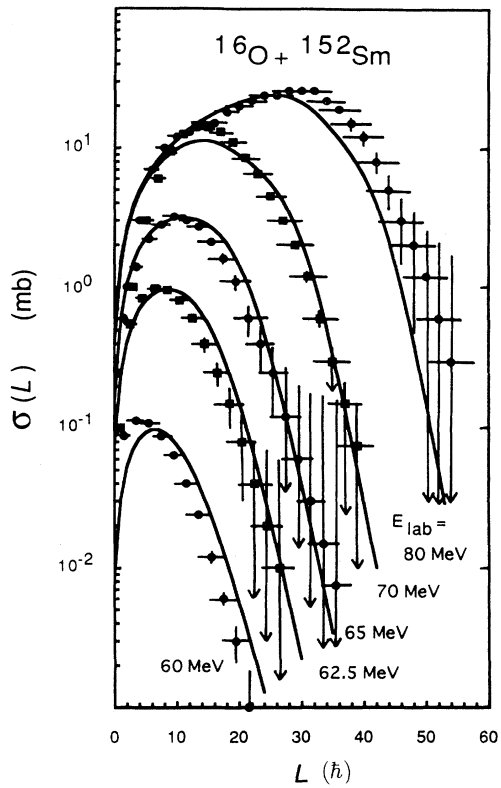

FIG. 12. Partial fusion cross sections calculated for the $^{16}O + ^{152}Sm$ system in comparison with the experimental data at E_{lab} = 60, 62.5, 65, 70, and 80 MeV [17].

There we observe a finer structure than that seen before in $D_{2\hbar}(E)$. At this moment, it is still premature to draw any definite conclusion, but nevertheless we might take it as a sign of the possibility that we might observe more detailed fine structure in $D(E)$, if the data become available with better accuracy.

E. L distribution of fusion cross sections and the average values

Figure 12 shows partial fusion cross sections $\sigma_F(\ell)$ calculated for the $^{16}O + ^{152}Sm$ system in comparison with

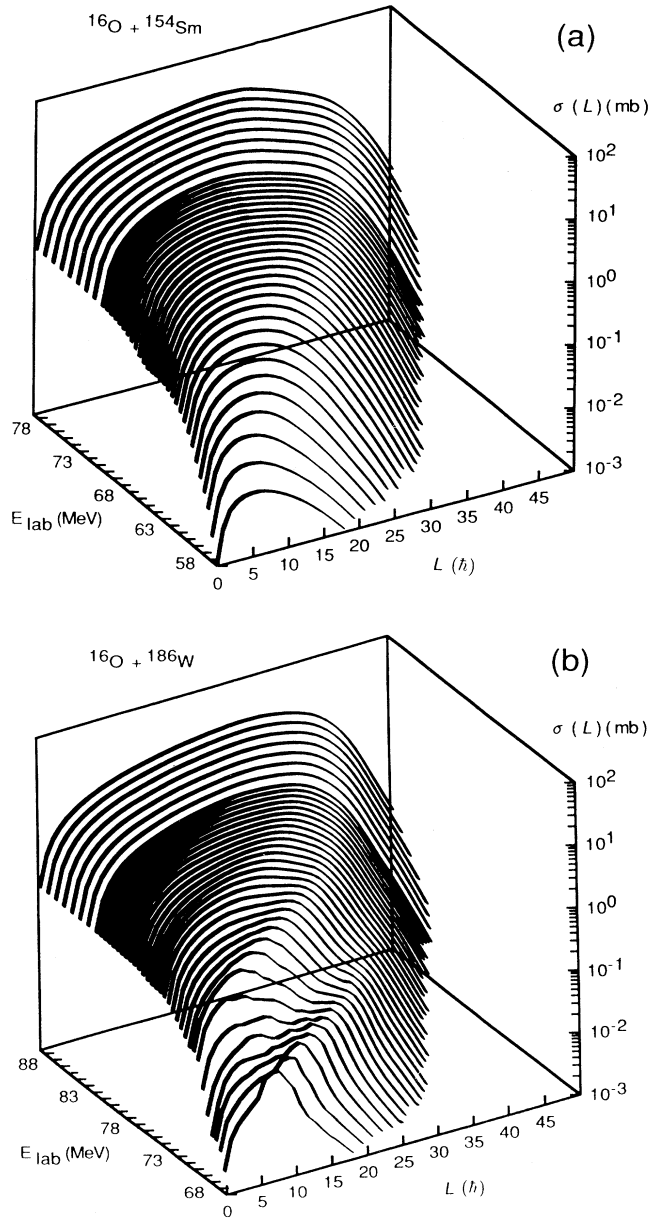

FIG. 13. Partial fusion cross sections calculated for the (a) $^{16}O + ^{154}Sm$ and (b) $^{16}O + ^{186}W$ systems as a function of E_{lab}.

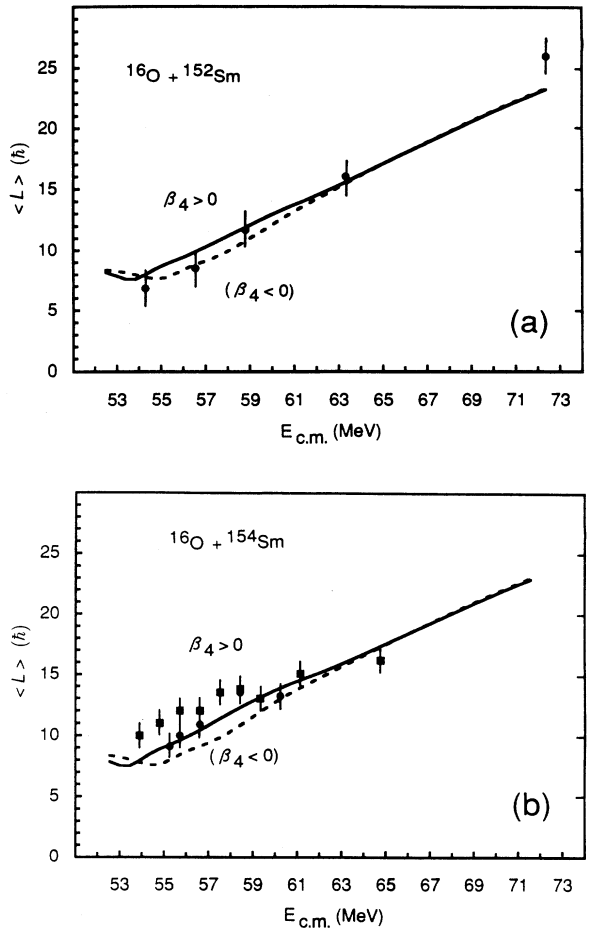

FIG. 14. Calculated average spin values $\langle L \rangle$ for (a) the $^{16}O + ^{152}Sm$ system and (b) the $^{16}O + ^{154}Sm$ system in comparison with the experimental data of Refs. [17,18], respectively. The dashed lines shown are the predictions obtained by reversing the sign of the β_4.

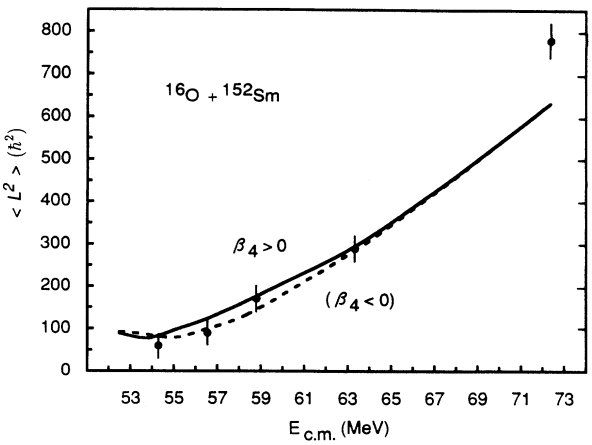

FIG. 15. $\langle L^2 \rangle$ averaged over partial fusion cross sections in the $^{16}O + ^{152}Sm$ system [17] are compared with the results from the coupled-channels calculation. The dashed line shows the predictions obtained by reversing the sign of β_4.

the experimental data [17]. The data are again well reproduced by the calculations.

In Fig. 13, we show two-dimensional plots of the partial fusion cross sections $\sigma_F(\ell, E)$ as functions of ℓ and E for (a) the $^{16}O+^{154}Sm$ system and (b) the $^{16}O+^{186}W$ system. An interesting aspect here is that a rather striking double structure develops in $\sigma_F(\ell, E)$ for the $^{16}O+^{186}W$ system. Such a structure is not seen in $D(E)$ of the $^{16}O+^{154}Sm$ system. We have noticed that the structure disappears when the absorption becomes stronger and also the absolute magnitude of the β_4 value is reduced. The structure also disappears when the sign of β_4 is reversed. These physical effects are exactly the same as those seen in the appearance of an additional peak in $D(E)$ of the $^{16}O+^{186}W$ system. This suggests that these two features have the same physical origin.

In Fig. 14, we present calculated average values of spin distribution $\langle L \rangle$ for the $^{16}O + ^{152,154}Sm$ systems in comparison with the experimental data [17,18]. The calculated $\langle L \rangle$ are again in good agreement with the measured values. In Fig. 15, comparison of the calculated $\langle L^2 \rangle$ with the existing data [17] is made for the $^{16}O + ^{152}Sm$ system. Again the agreement between the calculated and experimental values is good.

Finally, we present the calculated $\langle L \rangle$ for the $^{16}O + ^{186}W$ system in Fig. 16. Corresponding data are not available at present for this system.

F. Energy-dependent vs energy-independent potentials

So far, we have used optical potentials which are energy dependent. The energy dependence of the real and imaginary parts satisfies a dispersion relation (dispersive optical potentials). In Fig. 17, we show the fusion cross sections obtained when the energy dependence is ignored, i.e., when use is made of potential parameters fixed at $E = E_S$ (nondispersive potentials). As seen in the figure, the calculated σ_F with the nondispersive potentials overestimate the experimental σ_F by a factor of 2–3 at sub- and near-Coulomb barrier energies.

We observe a similar effect on the distribution of partial fusion cross sections as shown in Fig. 18. There σ_F calculated with the dispersive and nondispersive potentials are shown by the solid and dotted lines, respectively. When use of the nondispersive potential is made, the cross section becomes larger. For the $^{16}O + ^{186}W$ sys-

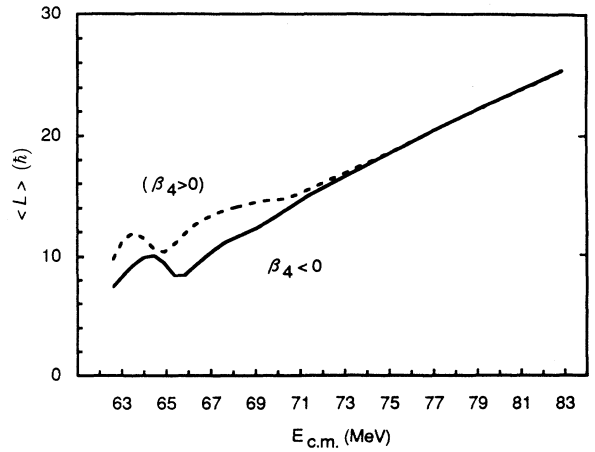

FIG. 16. Calculated average spin values $\langle L \rangle$ for the $^{16}O + ^{186}W$ system. The dashed line shows the predictions obtained by reversing the sign of β_4.

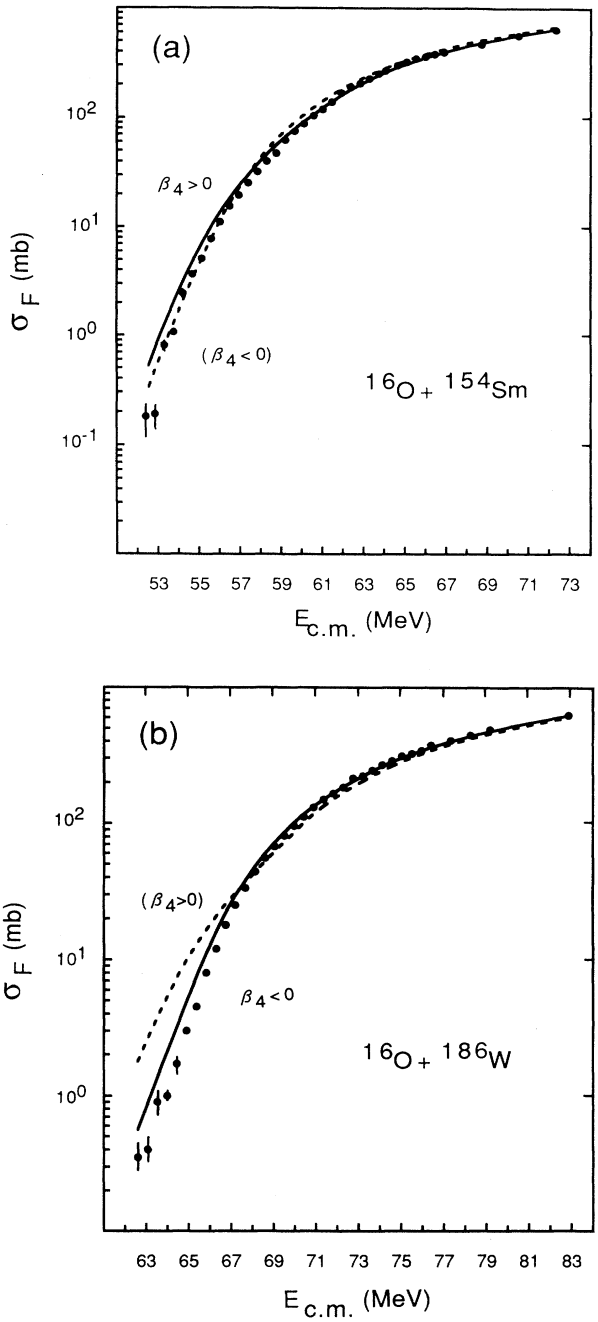

FIG. 17. Fusion cross sections for (a) $^{16}O + ^{154}Sm$ and (b) $^{16}O + ^{186}W$ systems calculated with nondispersive optical potential in comparison with the experimental data.

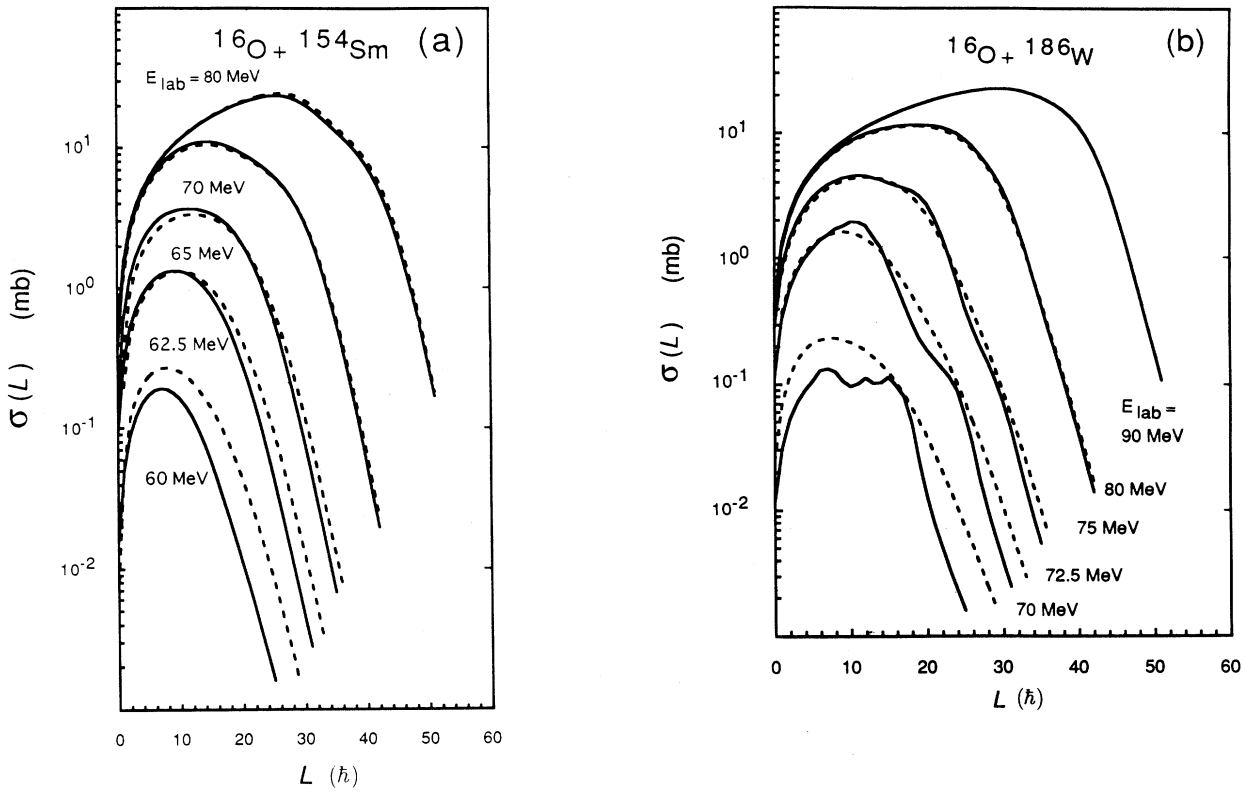

FIG. 18. Partial fusion cross sections calculated (a) for the ^{16}O + ^{154}Sm system at $E_{\rm lab}$ = 60, 62.5, 65, 70, and 80 MeV and (b) for the ^{16}O + ^{186}W system at $E_{\rm lab}$ = 70, 72.5, 75, 80, and 90 MeV. The dashed lines show the prediction obtained by neglecting the energy dependence of the optical potential.

tem, the wiggle seen in $D(E)$ at sub-Coulomb barrier energies disappears.

IV. CONCLUSION

We have performed extended CC calculations of fusion and scattering for the heavy-ion systems ^{16}O + ^{152,154}Sm, ^{18}O + ^{184}W, and ^{16}O + ^{186}W at sub- and near-Coulomb barrier energies. Use is made of dispersive optical potentials that satisfy the dispersion relation [20] in order to take into account the rapid energy dependence (threshold anomaly [4]) of the fusion potential (fusion part of the imaginary potential). The parameters of the fusion potential were determined from a fit of the calculated fusion cross sections to the data. The radius parameters thus fixed turned out to be rather large: $r_F \approx 1.4$ fm. It has been shown that calculations using such optical potentials can reproduce both fusion and scattering cross section data in a quantitative manner. The fusion data thus reproduced include not only the total fusion cross section, but also the partial ℓ distributions and the average spin ($\langle L \rangle$) values of the compound nuclei formed after fusion. It is remarkable that the fit obtained, particularly for the elastic and inelastic scattering data, is much better than that obtained in previous CC calculations using a small fusion radius parameter of $r_F = 1.0$ fm [5–7].

Further the calculations have been able to reproduce successfully the characteristic difference in the fusion-barrier distributions between the ^{16}O+^{154}Sm and ^{16}O+^{186}W systems in terms of the difference in the signs of β_4 of the above two heavy-ion systems. Note that a similar success has been obtained earlier in a study based on the adiabatic approximation [9].

The calculations have further indicated that the Y_4 deformation plays an important role in explaining characteristic features of other physical quantities, such as the interference pattern seen in the 4^+ inelastic scattering cross section and the enhancement of the average $\langle L \rangle$ values in the sub-Coulomb barrier energies observed in the ^{16}O+^{152,154}Sm systems.

It is remarkable that the 4^+ cross sections and the partial fusion cross section $\sigma_F(\ell)$ predicted for the ^{16}O+^{186}W show characteristic destructive interference patterns. These patterns originate from a large negative β_4 value that is experimentally well established in the α-particle scattering from ^{186}W [21]. At this moment, experimental data for testing the predictions are not available. It is desirable that such data will be collected in the future.

ACKNOWLEDGMENTS

We would like to express our sincere thanks to Professor R. W. Coker for his careful reading of the manuscript

and valuable comments. This work was supported in part by the U.S. Department of Energy under Contract No. DE-FG03-93ER40785. The numerical calculations were performed by using the CRAY Y-MP C90 at NERSC. One of the authors (T.I.) is grateful for the kind hospitality extended to him during his sabbatical stay at the Department of Physics, University of Texas at Austin and B.T.K. is supported by the Ministry of Education, Korea through BSRI-94-2422, and by KOSEF through the Center for Theoretical Physics, SNU.

[1] See, for instance, (a) *Proceedings of the International Workshop on Heavy-Ion fusion: Exploring the Variety of Nuclear Properties*, Padova, Italy, 1994 (in press); (b) *Proceedings of the RIKEN International Workshop on Heavy-Ion Reactions with Neutron-Rich Beams*, Riken, Wako, Japan, 1993, edited by M. Ishihara, N. Takigawa, and S. Yamaji (World Scientific, Singapore, 1993); (c) *Proceedings of the Workshop on Heavy Ion Collisions at Energies near Coulomb Barrier*, Daresbury Laboratory, England, 1990, edited by M. A. Nagarajan, IOP Conf. Series No. 110 (Institute of Physics and Physical Society, Bristol, 1991); (d) G. R. Satchler, Phys. Rep. **199**, 149 (1991).

[2] L. C. Vaz, J. M. Alexander, and G. R. Satchler, Phys. Rep. **69**, 373 (1981); J. R. Birkelund and J. R. Huizenga, Annu. Rev. Nucl. Part. Sci. **33**, 265 (1983).

[3] M. Beckerman, M. Salomaa, A. Sperduto, J. D. Molitoris, and A. DiRienzo, Phys. Rev. C **25**, 837 (1982); K. E. Rehm, F. L. H. Wolfs, A. M. van den Berg, and W. Henning, Phys. Rev. Lett. **55**, 280 (1985); A. M. Stefanini, G. Fortuna, R. Pengo, W. Meczynski, G. Montagnoli, L. Corradi, A. Tivelli, S. Beghini, C. Signorini, S. Lunardi, M. Morando, and F. Soramel, Nucl. Phys. **A456**, 509 (1986).

[4] J. S. Lilly, B. R. Fulton, M. A. Nagarajan, I. J. Thompson, and D. W. Banes, Phys. Lett. **151B**, 181 (1985); B. R. Fulton, D. W. Banes, J. S. Lilly, M. A. Nagarajan, and I. J. Thompson, *ibid.* **162**, 55 (1985).

[5] S. Landowne and S. C. Pieper, Phys. Rev. C **29**, 1352 (1984); S. C. Pieper, M. J. Rhoades-Brown, and S. Landowne, Phys. Lett. **162B**, 43 (1985).

[6] G. R. Satchler, M. A. Nagarajan, J. S. Lilley, and I. J. Thompson, Ann. Phys. (N.Y.) **178**, 110 (1987).

[7] H. Esbensen and S. Landowne, Nucl. Phys. **A492**, 473 (1989); H. Esbensen, S. H. Fricke, and S. Landowne, Phys. Rev. C **40**, 2046 (1989); R. J. Tighe, J. J. E. Aguilera, G.-B. Liu, A. Morsad, J. J. Kolata, S. H. Fricke, H. Esbensen, and S. Landowne, *ibid.* **42**, 1530 (1990); S. H. Fricke, H. Esbensen, and S. Landowne, *ibid.* **45**, 1500 (1992).

[8] J. X. Wei, J. R. Leigh, D. J. Hinde, J. O. Newton, R. C. Lemmon, S. Elfstrom, J. X. Chen, and N. Rowley, Phys. Rev. Lett. **67**, 3368 (1991).

[9] R. C. Lemmon, J. R. Leigh, J. X.Wei, C. R. Morton, D. J. Hinde, J. O. Newton, J. C. Mein, M. Dasgupta, and N. Rowley, Phys. Lett. B **316**, 32 (1993).

[10] P. H. Stelson, Phys. Lett. B **205**, 190 (1988).

[11] N. Rowley, G. R. Satchler, and P. H. Stelson, Phys. Lett. B **254**, 25 (1991).

[12] M. A. Nagarajan, N. Rowley, and R. Lindsay, J. Phys. G **12**, 529 (1986).

[13] T. Udagawa and T. Tamura, Phys. Rev. C **29**, 1922 (1984); T. Udagawa, B. T. Kim, and T. Tamura, *ibid.* **32**, 124 (1985).

[14] R. G. Stokstad and E. E. Gross, Phys. Rev. C **23**, 281 (1981).

[15] C. E. Thorn, M. J. LeVine, J. J. Kolata, C. Flaum, P. D. Bond, and J.-C. Sens, Phys. Rev. Lett. **38**, 384 (1977).

[16] P. Talon, N. Alamanos, M. Lamehi-Rachti, C. Levi, and L. Papineau, Nucl. Phys. **A359**, 493 (1981).

[17] A. H. Wuosmaa, R. R. Betts, B. B. Back, M. P. Carpenter, H. Esbensen, P. B. Fernandez, B. G. Glagola, Th. Happ, R. V. F. Janssens, T. L. Khoo, E. F. Moore, F. Scarlassara, and Ph. Benet, Phys. Lett. B **263**, 23 (1991).

[18] S. Gil, R. Vandenbosch, A. Charlop, A. Garcia, D. D. Leach, S. J. Luke, and S. Kailas, Phys. Rev. C **43**, 701 (1991).

[19] T. Tamura, Rev. Mod. Phys. **37**, 679 (1965).

[20] C. Mahaux, H. Ngo, and G. R. Satchler, Nucl. Phys. **A449**, 354 (1986); **A456**, 134 (1986).

[21] D. L. Hendrie, Phys. Rev. Lett. **31**, 478 (1973).

[22] T. Udagawa and B. T. Kim, Phys. Rev. C **40**, 2271 (1989).

[23] B. T. Kim and T. Udagawa, Phys. Rev. C **42**, 1147 (1990).

[24] B. T. Kim, Phys. Lett. **80**, 353 (1979).

[25] T. Izumoto, Y.-W. Lui, D. H. Youngblood, T. Udagawa, and T. Tamura, Phys. Rev. C **24**, 2179 (1981).

[26] W. G. Love, T. Terasawa, and G. R. Satchler, Nucl. Phys. **A291**, 183 (1977).

[27] B. T. Kim, T. Udagawa, and T. Tamura, Phys. Rev. C **33**, 370 (1986).

[28] I. Y. Lee, J. X. Saladin, J. Holden, J. O'Brien, C. Baktash, C. Bemis, Jr., P. H. Stelson, F. K. McGowan, W. T. Milner, J. L. C. Ford, Jr., R. L. Robinson, and W. Tuttle, Phys. Rev. C **12**, 1483 (1975).